Article

Triple-Pair Constellation Configurations for Temporal Gravity Field Retrieval

Anna F. Purkhauser *[iD] and **Roland Pail**[iD]

Chair of Astronomical and Physical Geodesy, Technical University of Munich, Arcisstraße 21, 80333 Munich, Germany; roland.pail@tum.de

* Correspondence: anna.purkhauser@tum.de; Tel.: +49-89-289-231-81

check for updates

Abstract: The goal of next-generation gravity missions (NGGM) is to improve the monitoring of mass transport in the Earth system by an increased space-time sampling capability as well as higher accuracies of a new generation of instrumentation, but also to continue the monitoring time series obtained by past and current missions such as GRACE and GRACE Follow-On. As the likelihood of three satellite pairs being simultaneously in orbit in the mid-term future increased, we have performed a closed-loop simulation to investigate the impact of a third pair in either polar or inclined orbit as an addition to a Bender-type constellation with NGGM instrumentation. For the additional pair, GRACE-like as well as NGGM instrumentation was tested. The analysis showed that the third pair mainly increases the redundancy of the monitoring system but does not significantly improve de-aliasing capabilities. The best-performing triple-pair scenario comprises a third inclined pair with NGGM sensors. Starting with a Bender-type constellation of a polar and an inclined satellite pair, simulation results indicate an average improvement of 11% in case of adding the third pair in a near-polar orbit, and of 21% for the third pair placed in an inclined orbit. The most important advantage of a multi-pair constellation, however, is the possibility to recover daily gravity fields with higher spatial resolution. In the case of the investigated triple-pair scenarios, a meaningful daily resolution with a maximum spherical harmonic degree of 26 can be achieved, while a higher daily parametrization up to degree 40 results in spatial aliasing and thus would need additional constraints or prior information.

Keywords: future gravity missions; time variable gravity; near-real time; numerical simulation; spherical harmonics

1. Introduction

Dedicated gravimetric satellite missions like the Challenging Minisatellite Payload (CHAMP; [1]) and the Gravity Recovery and Climate Experiment (GRACE; [2]) and GRACE Follow-On (FO; [3]) missions have been providing, for nearly two decades, essential observations of the changes of the Earth's gravity field on a global scale. This monitoring is fundamental for applications in Earth sciences, such as hydrology [4], atmosphere [5], plate tectonics [6], earthquakes [7], and glacial isostatic adjustment (GIA; [8]) as well as cryosphere [9,10].

The GRACE-FO mission was launched in May of 2018 to continue monitoring the temporal gravity field of the Earth, after the GRACE mission was decommissioned due to a battery failure at the end of 2017. However, the observed data from GRACE/GRACE-FO have limitations regarding spatial and temporal resolution, homogeneity, as well as sensitivity. The user requirements collected by [11] underline the need for long-term, sustained gravity observations with increased spatial and temporal resolution to observe small-scale, short-time mass transport phenomena.

To find optimal mission concepts with improved spatial and temporal resolutions, various studies have been performed: The authors of [12–16] investigated the performance of single-pair missions. The authors of [17–20] analyzed flying a second inclined pair in addition to an in-line pair in polar orbit (furthermore called Bender-type constellation), thus improving the space-time sampling and having available multi-directional observations as compared to a single polar-pair due to the two different orbit planes.

Mission proposals in response to European Space Agency (ESA) Earth Explorer calls 8, 9, and 10 like e.motion with a single pair in a pendulum constellation [21], e.motion2 [22] based on a Bender-type concept, or the innovative high–low tracking formation mission MOBILE [23] also achieve improved error characteristics. While the e.motion and e.motion2 mission proposals are based on the observation system of low-low satellite-to-satellite tracking (LL-SST) as implemented in GRACE and GRACE-FO, the MOBILE concept proposes a different observation strategy of high-precision high–low tracking as well as new instrumentation. All three proposals emphasize the need for continuous and sustained observations of the Earth's mass transport on a global scale from space.

A study by [24] has concluded that the gain in accuracy of the Bender double-pair constellation is higher compared with the single-pair pendulum formation and is therefore preferred. The ESA-funded SC4MGV study (Assessment of Satellite Constellations for Monitoring the Variations in Earth Gravity Field, [15]) found that there is a certain degree of freedom in the orbit design of Bender-type mission concepts. In the follow-on ESA-study ADDCON (Additional Constellation and Scientific Analysis of the Next Generation Gravity Mission Concept; [25]) an analysis regarding orbit height and instruments showed that a Bender pair with improved instrumentation gave the best results for a seven-day reference solution [26].

In the context of observing short period signals within short latencies, daily solutions in near-real time are needed. However, the potential to use the retrieved gravity fields for applications with high temporal variations, like hydrology and earthquake monitoring, is limited by the requirement to recover gravity field variations as detailed as possible, i.e., with highest spatial resolution. An increase in temporal resolution means less observations per analysis period and therefore a reduced redundancy in the parameter estimation process. For possible NGGM constellations with at least two pairs, the co-estimation of long-wavelength gravity field solutions for short time periods such as one day, further called Wiese approach, was successfully tested in closed-loop simulations [20,27].

As various space agencies are considering flying a GRACE-like or NGGM mission, the potential of triple pairs compared to a Bender-type double pair is of interest. The most significant advantage of an additional pair to a Bender-type constellation, apart from an improved performance, is the possibility to increase and resolve daily Wiese solutions with higher spatial resolution. Additionally, for time-critical monitoring applications (e.g., early-warning and forecasting systems) information in near-real time (NRT) is of essence, meaning an NRT processing scheme [28] is necessary. This paper evaluated three scenarios with two and three pairs and analyses their potential for NRT processing and the highest possible daily resolution for applications such as the monitoring of hydrological extremes such as droughts and floods.

The paper is organized as follows: Section 2 reviews the satellite mission design as well as the space-time sampling of various applications. The methodology of the full-scale closed-loop simulation, based on the software available at the Institute of Astronomical and Physical Geodesy (IAPG) of the Technical University Munich (TUM), is described in Section 3. Section 4 contains the obtained gravity results in the spatial as well as the frequency domain, and finally, the conclusions regarding the possible improvements on gravity field as well as on application level are presented in Section 5.

2. Constellation Design

2.1. Orbit Constellation

Two orbits are the basis to form double- and triple-pair constellations. In Table 1, the general information regarding the used orbits is listed. The letter "p" represents the polar orbit, while the letter "i" stands for the inclined orbit. These letters are also used for the scenario description within the paper later on. Both orbits have a seven-day repeat cycle and a drift rate of 1.3°/cycle. The resulting homogeneous ground track coverage allows for stable seven-day gravity field solutions. Additionally, the dense ground track spacing over longer periods due to the drifting orbit design allows for a high-degree gravity field recovery for more extended periods according to the Nyquist–Colombo sampling rule for space-borne gravimetry [29,30].

Table 1. Basic information on the simulated orbits forming the constellations.

Orbit	Altitude	Inclination	Repeat Cycle	Drift Rate
Polar (*p*)	~340 km	89°		
Inclined (*i*)	~ 355 km	70°	7 days	1.3° / cycle

Figure 1 shows a 3D and a schematic view of the analyzed in-line satellite pair constellations based on the Bender double-pair. The Bender double-pair constellation is comprised of a near-polar pair and an inclined pair with an inclination of 70°. The polar pair is placed in an orbit plane with an ascending node of 0°, and the inclined pair in an orbit plane with an ascending node of 90°. The polar gap of the inclined pair (orbit ground tracks in red) is clearly visible at the North Pole. This basic Bender constellation, also described in Table 2, is assumed to have an improved set of sensors on board (see Section 3.2).
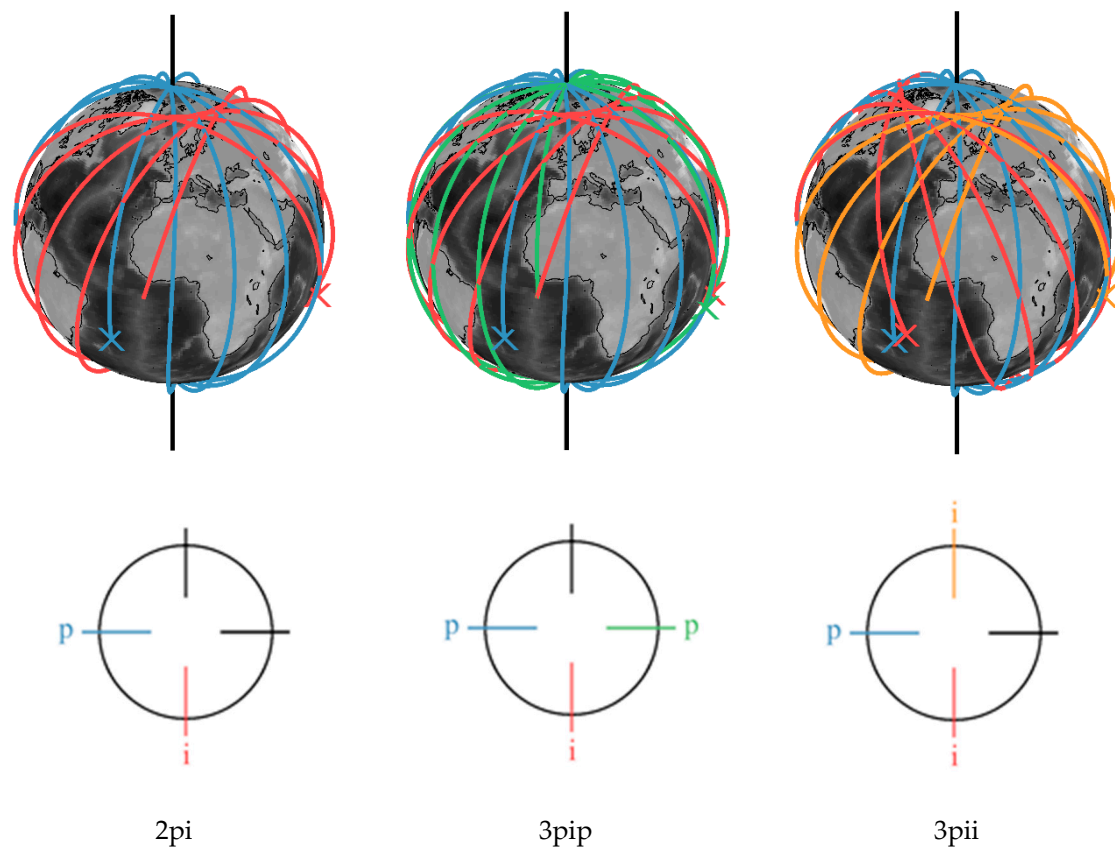
Figure 1. Constellations of in-line satellite pairs. (2pi) Bender double-pair, (3pip) triple-pair with additional polar pair, (3pii) triple-pair with additional inclined pair.

Table 2. Scenario description with the angle of the ascending node (Ω) included. Acronyms for polar (p) and inclined (i) are used.

Scenario	Description	Ω_1	Ω_2	Ω_3
2pi	Double-pair, Bender (NGGM noise)	0°	90°	
3pip *a* *b*	Triple-pair, Bender + polar 3rd pair GRACE-like noise 3rd pair NGGM noise	0°	90°	180°
3pii *a* *b*	Triple-pair, Bender + inclined 3rd pair GRACE-like noise 3rd pair NGGM noise	0°	90°	270°

The third pair is then placed in an orbit plane that is perpendicular to the orbit plane of the already existing polar or inclined pair. In case of triple-pair scenario 3pip, this means a second polar pair with an ascending node of 180°, and in case of triple-pair scenario 3pii, it means a second inclined pair with an ascending node of 270° (cf. Table 2) and the same inclination as the first inclined pair. The added satellite pairs are equipped with sensors featuring either a GRACE-like (a) or NGGM (b) noise (see Section 3.2). Through this distribution, an optimal spatial and temporal resolution is enabled, which is especially relevant for the aspired daily solution with the highest possible spatial resolution.

2.2. Space-Time Sampling

Science requirements for applications in solid Earth, hydrology, ocean, ice, atmosphere, and corresponding science fields were collected by [31] and visualized in 2D bubble plots; see Figure 2. The extent of the bubbles visualizes an estimation of the necessary temporal and spatial

resolution to enable their observation and, subsequently, the monitoring by gravity satellite mission constellation. The bubbles together with the expected temporal and spatial resolution of the satellite mission gives a good first indication if a mission is able to observe specific features. In Figure 2, the possible performance of double (blue) and multi-pair (light green) constellations is visualized. The lines are a combination of the published original diagram in [31] and the ground tracks as well as results of the presented scenarios. However, it has to be stated that a general statement like the shown bubble plot is only a rough indication. Additionally, the observability also depends on the signal amplitude, which is not considered in Figure 2.
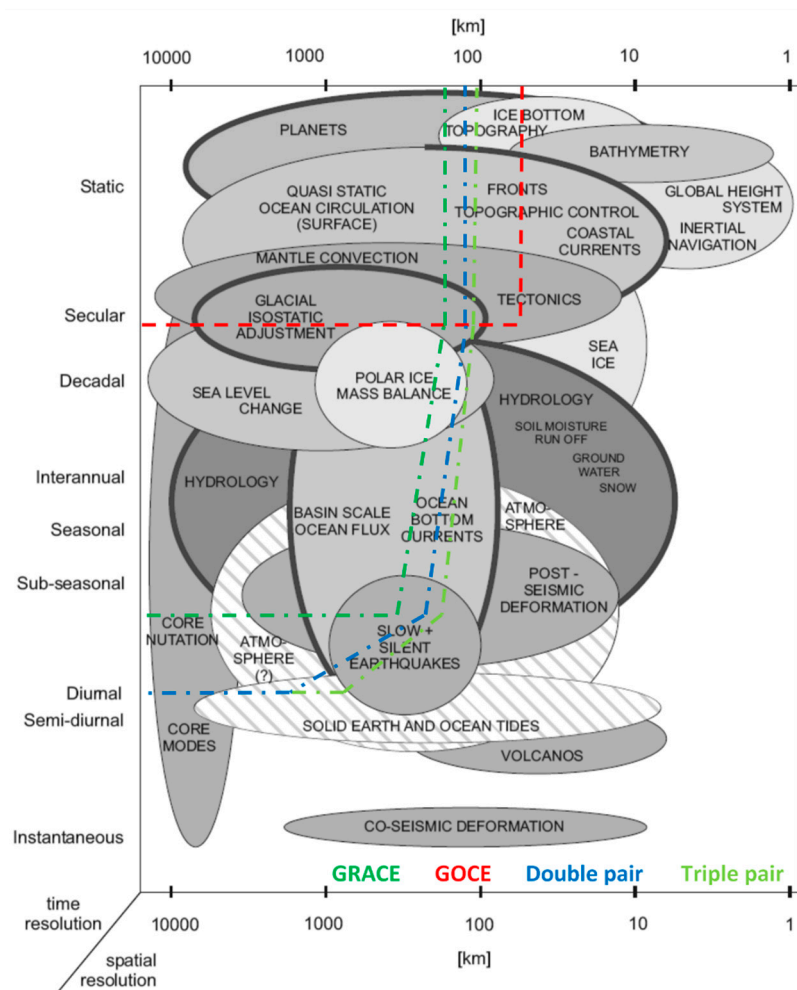

Figure 2. Temporal and spatial scales of time-varying gravity field as well as the spatial and temporal limits of Gravity Recovery and Climate Experiment (GRACE), Gravity field and steady-state ocean circulation explorer (GOCE), and possible next-generation gravity missions (NGGM) constellations. Based on [31].

After the successful exploitation of CHAMP, GRACE, and GOCE (Gravity field and steady-state ocean circulation explorer) and the additional knowledge based on their observations, various studies on necessary accuracies of future gravity fields were published. The authors of [11] collected updated science and user needs by a panel of scientists representing the main fields of application of possible NGGM concepts to form consolidated requirements for a compromise of all applications with the possibility to optimize for a specific field of application.

One of the major problems of a GRACE-like single-pair mission is temporal aliasing of high-frequency mass transport signals that are mainly due to processes in the atmosphere and the oceans, which cannot be captured due to the limited temporal resolution of the mission. This requires a-priori

atmosphere and ocean (AO) de-aliasing based on external models. These temporal aliasing effects are significantly reduced by multi-pairs, e.g., [20] investigated the capabilities of Bender double-pair constellations to observe the full AOHIS (atmosphere, ocean, hydrology, ice, and solid Earth) signal instead of a-priori modelling of AO and the estimation of the hydrology, ice, and solid Earth (HIS) components only. Lastly, the anisotropic error behavior that is typical for GRACE-like solutions is a well-known phenomenon and typically treated with different filter approaches [32–34]. Multi-pair constellations inherently have additional observations and especially the addition of observations in an inclined orbit, as in the Bender-type constellation, add signal content and improve the anisotropic error behavior, and therefore decrease the GRACE striping significantly.

3. Closed-Loop Simulation

3.1. Numerical Simulator

The full-scale gravity field estimation software [35,36] available at the IAPG was used to execute the closed-loop simulations. The numerical orbit integration follows a multistep method for the numerical integration according to [37] with a modified divided difference form of the Adams Predict-Evaluate-Correct-Evaluate (PECE) formulas and local extrapolation [38].

In the generation of the dynamic models, the static gravity field GOCO05s model [39] up to maximum expansion degree and order (d/o) 120 is included. To simulate the non-tidal time-varying gravity field due to mass change, the updated Earth System Model (ESM) of ESA [40], furthermore called reference AOHIS, is used as reference world. The differences of the ocean tide (OT) model GOT4.7 (Goddard Ocean Tide) model [41] and the EOT11a (Empirical Ocean Tide) model [42] are used to replicate the ocean tide model errors.

The functional model follows the typical formulation used for LL-SST missions like GRACE (cf. Table 3). The "true" dynamic orbits as well as the "true" GNSS HL-SST and LL-SST observations are additionally superimposed by the noise models described in Section 3.2 depending on the scenario. The impact of orbit errors on the gravity field processing is taken into account by propagating 1 cm white noise of the integrated orbit positions of each satellite.

Table 3. Force and noise models of the "true" and "reference" world used in the full-scale simulations.

Model	"True" World	Reference World
Static gravity field (GF) model	GOCO05s	GOCO05s
Time varying GF model	AOHIS	-
Ocean tide model	EOT11a	GOT4.7
Noise model	SST, acc. noise	-

The assembling of the NEQ systems is done with spherical harmonics (SH) base functions of the Earth's gravitational potential V and is expressed by the series expansion [43]:

$$V(r, \theta, \lambda) = \frac{GM}{a} \sum_{n=0}^{\infty} \left(\frac{a}{r}\right)^{n+1} \sum_{m=0}^{n} \overline{P}_{nm}(cos\theta)\left(\overline{C}_{nm}cosm\lambda + \overline{S}_{nm}sinm\lambda\right), \tag{1}$$

where *GM* represents the product of the gravitational constant and the Earth's mass, a the semi-major axis of the Earth, $\overline{P}_{nm}$ is the fully normalized Legendre polynomial of degree *n* and order *m*, $\overline{C}_{nm}$ and $\overline{S}_{nm}$ are the fully normalized SH coefficients, and the location is given by the radius r (geocentric distance of the satellite), geocentric co-latitude *θ*, and longitude *λ*.

The stochastic model is approximated for each satellite pair individually by using a combination of digital Butterworth ARMA filters [44,45] that best represent the amplitude spectral density (ASD) of the pre-fit residuals of a noise-only computation. Assuming uncorrelated high–low and low–low SST observations, weighting matrices are set up for all observation components separately.

The gravity field parameters are estimated by solving full normal equations of a least-squares system based on a standard Gauss–Markov model using weighted least squares with stochastic models following the simulated instrument noise levels. From the resulting gravity field coefficients, the average of the true mass transport model from the same period is removed to enable the analyses of quality and performance of the gravity retrieval.

3.2. Noise

While the basic Bender-type constellation is assumed to have a set of improved sensors, the additional satellite pairs are simulated with a GRACE-like or a NGGM noise setting. The GRACE-like noise represents a noise level of accelerometer (ACC) and satellite-to-satellite tracking (SST) resembling the error characteristics of the instruments implemented on the GRACE mission, and an NGGM noise scenario with improved ACC and laser ranging interferometer (LRI) noise characteristics. The HL-SST observable always has the same white noise of 1 cm propagated along the orbit. The satellites are assumed to fly in drag-compensation mode in approximately 350 km orbit altitude so that the most significant parts of the non-gravitational forces are compensated by a propulsion system consisting of ion thrusters.

3.2.1. GRACE-Like Noise

An analytical noise model characterizes the main measurement unit, the K-Band Ranging system (KBR) to observe the inter-satellite distances. The ASD describes the noise model analytically and is expressed in terms of range rates (rr) [17],

$$d_{rr} = 2 \cdot 10^{-6} \cdot 2\pi f \sqrt{\left(\frac{10^{-2} Hz}{f}\right)^2 + 1} \frac{m}{s \sqrt{Hz}}, \tag{2}$$

where f is defined as frequency. The on-board accelerometer senses the linear non-gravitational accelerations and the angular accelerations acting on the satellites with air drag being the main contributor. The ACC is modeled after [46].

3.2.2. NGGM Noise

In the case of NGGM noise, the principal measurement is observed by the laser interferometry instrument, meaning an improvement of factor 100

$$d_{rr} = 2 \cdot 10^{-8} \cdot 2\pi f \sqrt{\left(\frac{10^{-2} Hz}{f}\right)^2 + 1} \frac{m}{s \sqrt{Hz}}. \tag{3}$$

Additionally, an improved accelerometer is implemented

$$d_{acc.\ x} = d_{acc.\ z} = 10^{-11} \sqrt{\frac{\left(\frac{10^{-3} Hz}{f}\right)^4}{\left(\left(\frac{10^{-5} Hz}{f}\right)^4 + 1\right)} + 1 + \left(\frac{f}{10^{-1} Hz}\right)^4} \frac{m}{s^2 \sqrt{Hz}}, d_{acc.\ y} = 10 \cdot d_{acc.\ z} \tag{4}$$

with x being the along-track, y is across-track, and z is the quasi-radial component. The error assumption was provided by the consultancy support of Thales Alenia Space Italia (TAS-I).

4. Results

We calculated eight seven-day solutions for January and February 2002 with the numerical closed-loop simulation software described in Chapter 3 for the double (estimated until d/o 70) and triple (estimated until d/o 90) pairs defined in Table 2. All scenarios were processed with the Wiese

approach, which co-parametrizes low-resolution daily gravity field solutions and longer-term gravity field solution. For the evaluation of long-term applications, the time series was extended to one year for selected scenarios and processed with the NRT approach. In order to summarize the results and to simplify the corresponding figures, the shown degree root mean square (RMS) errors always represent the average degree RMS of all estimated seven-day solutions.

We compared the results in the spatial as well as the frequency domain. The gravity field was transformed to equivalent water heights (EWH). In terms of degree RMS signal/errors, this means

$$\sigma_n(EWH) = \frac{a\rho_e}{3\rho_w} \frac{2n+1}{1+k_n} \sqrt{\sum_{m=0}^{n} \left(c_{nm}^2 + s_{nm}^2\right)}, \tag{5}$$

where ρ_w and ρ_e represent the average density of water and Earth, a the semi-major axis of the Earth, k_n is the Love numbers, and c_{nm} and s_{nm} represent the SH coefficients or coefficient differences to the true solution [47,48].

4.1. Double vs. Triple Pairs

In this section, we compare the achievable performance of double pair and triple-pair scenarios. Figure 3 shows degree RMS curves for the double pair (estimated up to d/o 70) and the triple-pair (estimated up to d/o 90) scenarios as defined in Table 2 in terms of an average of the seven-day solutions of the two-monthly observation period. Daily spherical harmonic coefficients (Wiese parameters) up to d/o 15 were co-estimated, as recommended by [28]. The double pair scenarios 2pi in blue is shown as a reference. The triple-pair scenarios 3pip with the third pair being in a polar orbit (red and green) exhibited small improvements, especially in the lower degrees. Additionally, the crossover between signal and errors degree RMS curves was approximately 5 degrees higher than for the reference double pair scenario. The best performance is visible for scenario 3pii,b with the third pair in an inclined orbit and also laser instrumentation for the SST (lilac curve). With this constellation, the performance in terms of spatial resolution can be improved by 10 degrees compared to the double pair.
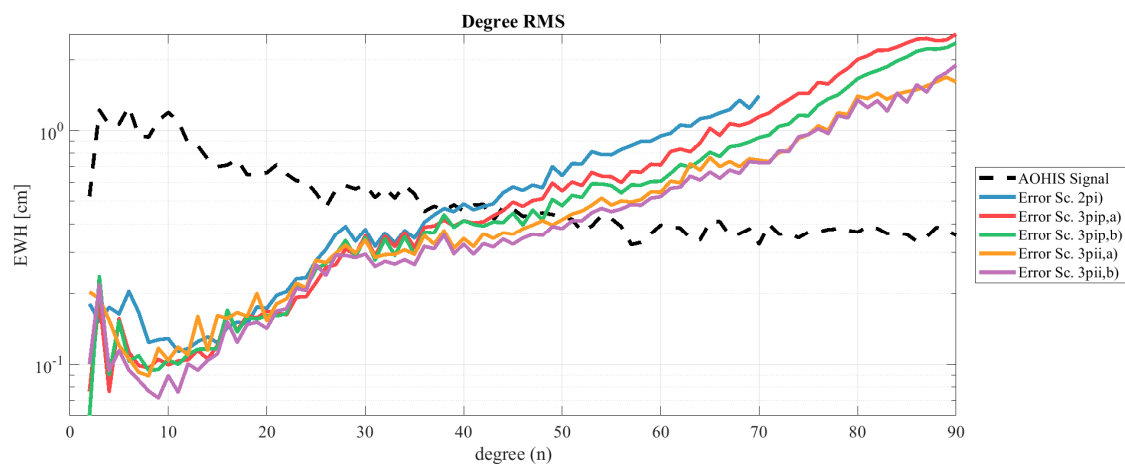

Figure 3. Degree root mean square (RMS) of double pair (estimated until d/o 70) vs. triple pair (estimated until d/o 90) scenarios of the whole solution. Daily Wiese solution estimated until d/o 15.

Figure 4a shows coefficient differences of the second solution (08/01/2002 to 14/01/2002) with respect to the reference AOHIS signal for the true reference of scenario 2pi (computed up to d/o 70), 3pip, and 3pii (computed up to d/o 90) for noise scenario b (NGGM noise). Obviously, the main gain in performance of the triple-pairs scenario 3pii including two inclined pairs occurred in the sectorial and near-sectorial coefficients, expressing the improved de-striping capabilities of this constellation. Figure 4b shows the spatial representation of these differences of the recovered and the true solution in

terms of EWH difference grids up to d/o 50 due to the crossover of the signal and error curve in Figure 3. The improved performance of scenario 3pii can be seen especially in the spatial representation in Figure 4b. Compared to the other scenarios, the striping effect was reduced, but still visible. In Table 4, the cumulative errors in centimeters EWH of selected upper maximum d/o 10 to 50 are provided. While a third polar pair showed only small improvements of about 5% to 10% compared to the Bender double pair scenario 2pi, a second inclined pair resulted in significantly improvements of about 20% to 40%. The expected improvement of the square-root-n rule led to an expected improvement of 22%, reached by the second inclined pair.
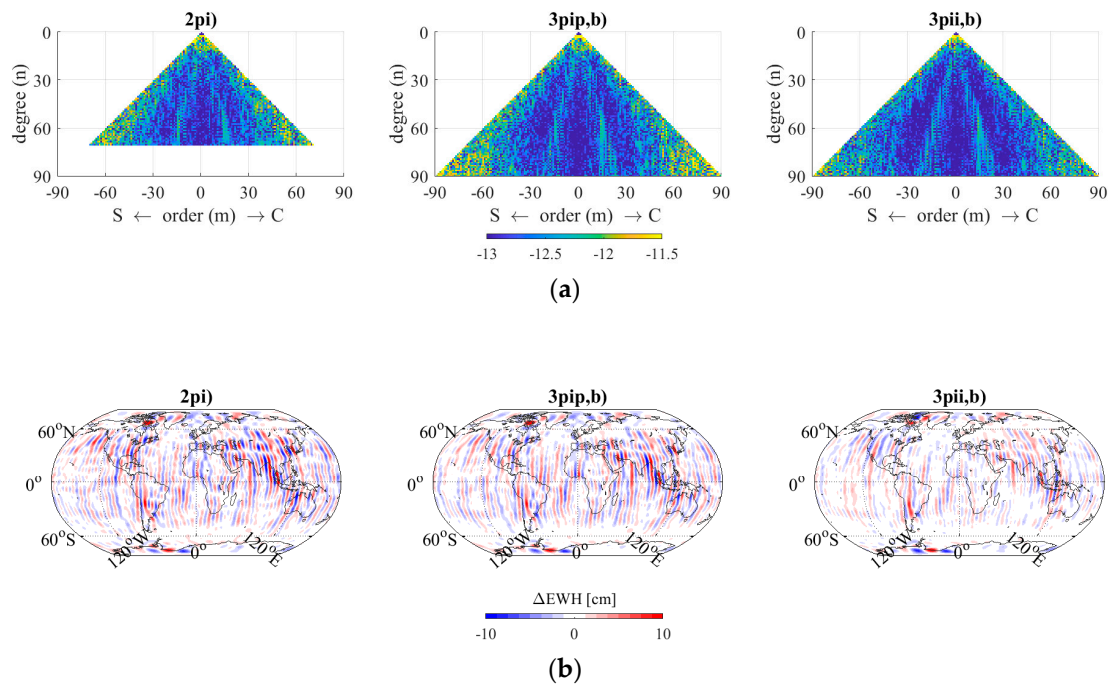

Figure 4. Double- vs. triple-pair scenarios (solution from 08/01/2002 to 14/01/2002). (**a**) Coefficient differences of scenario 2pi (computed up to d/o 70), 3pip, and 3pii (computed up to d/o 90) with all sensors set to the NGGM noise. (**b**) Spatial representation in terms of equivalent water heights (EWH) differences to the true solution up to d/o 50.

Table 4. Cumulative error in cm EWH of scenarios at different maximum d/o from 10 to d/o 50 (latest crossing point of signal and error curve).

Scenario // Cumulative Error at	d/o 10	20	30	40	50 in [cm] EWH
2pi	0.60	0.75	1.15	1.73	2.58
3pip,a	0.55	0.71	1.17	1.78	2.48
3pip,b	0.55	0.71	1.18	1.79	2.48
3pii,a	0.47	0.65	1.06	1.50	1.96
3pii,b	0.38	0.53	0.91	1.32	1.74

Spatial representations of the improvements of the triple pairs compared to the double pair solution are shown in Figure 5, which depicts the difference of the estimated to the reference solution of the best solution. For this, we analyzed an EWH difference grid up to d/o 50 for a seven-day solution and computed the difference of the estimated and reference field for every point of the grid. Blue means the double pair scenario 2pi had the smaller difference value, thus was closer to the reference and visualized in the figure, while red means the respective triple-pair scenario 3pip,b or 3pii,b had the smaller difference value and was closer to the truth and visualized. When comparing scenario 3pip,b with the double pair (Figure 5a), a clear improvement of the triple-pair scenario was not apparent.

While in Canada, the triple pair had a lower difference value, the double pair performed better over Antarctica. Overall, the triple pair had lower difference values in the Northern hemisphere, while in the Southern part, an ambiguous picture was visible.
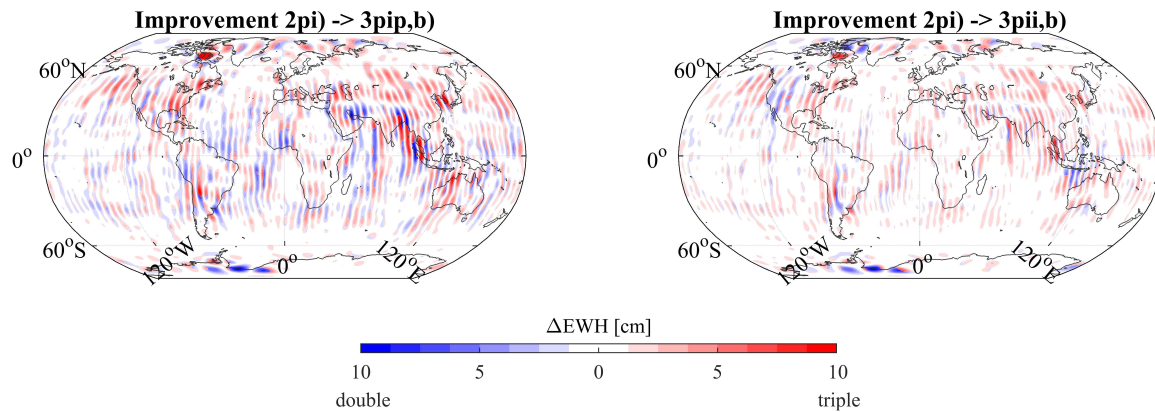

Figure 5. Difference of estimated vs. reference solution (up to d/o 50) of triple-pair scenarios 3pip,b and 3pii,b compared to double pair scenario 2pi in EWH [cm] of the seven-day solution from 08/01/2002 until 14/01/2002. Red means the triple-pair scenarios are closer to the truth, blue means the double pair scenario is closer to the truth. (**a**) Comparison of double pair scenario 2pi to triple-pair scenario 3pip,b. (**b**) Comparison of double pair scenario 2pi to triple-pair scenario 3pii,b.

Scenario 3pii,b compared to the double pair (Figure 5b) showed a significant improvement for the triple-pair scenario. The double pair was only better than the triple-pair scenario in a few limited areas. Also, the overall magnitude of the difference decreased. The anisotropic error behavior of a classic GRACE-like near-polar pair was further reduced by the second inclined pair. Such a constellation came, however, with the drawback of only one near-polar pair, which was the basis of every temporal gravity field mission so far. The near-polar pair is important as the ground track has the best global coverage. If the polar pair failed, the polar areas would not be observed at all by the remaining constellation. Within the processing, a regularization would have to be applied if global base functions such as SH are used for parameterization.

Although both triple-pair scenarios had the same amount of observations, the third inclined pair's along-track observations added more information, further reducing the variability between $-60°$ and $60°$ latitude. The variability decreased in scenario 3pii,b, and not only in the area covered by the inclined pairs, but also in the polar region covered by only one near-polar pair. The result shows that the introduction of the third pair in an inclined orbit in scenario 3pii,b adds relevant signal and stabilizes the solution overall.

In Figure 6, the standard deviation of the difference between the simulated and the reference solutions over the whole computation period (one year), furthermore called RMS variability, of both triple-pair scenarios is visualized. For each grid point, the RMS variability value over the time period is shown. The higher the RMS variability, the darker red the grid point is colored. A detail of the Pacific Ocean is selected as this is an area of little to no temporal gravity signal. The result again shows a decreased striping pattern in scenario 3pii,b in Figure 6b compared to scenario 3pip,b in Figure 6a. The reduced striping pattern is therefore a result of the improved instrument noise and the better observation geometry. The RMS variability is reduced significantly from 2.24 cm EWH to 1.7 cm EWH globally for scenario 3pii,b, supporting the previous statement.
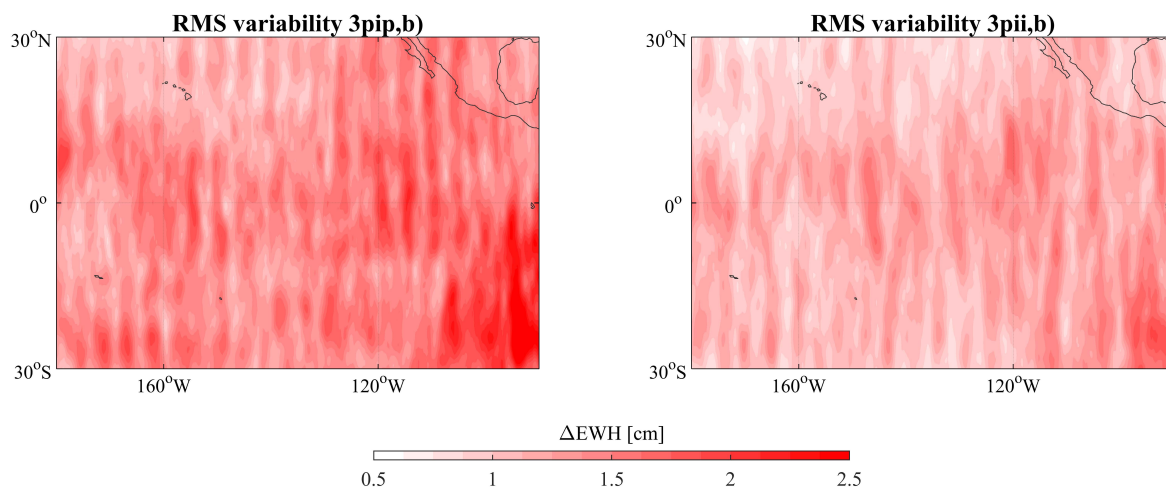
Figure 6. RMS variability over one year of triple-pair scenarios. Standard deviation computed from reference minus estimated solution until d/o 50. (**a**) RMS variability detail of triple-pair scenario 3pip,b. (**b**) RMS variability detail of triple-pair scenario 3pii,b.

To visualize the impact of the daily parametrization on the double pair scenario, Figure 7a shows degree RMS curves of double pair scenario 2pi (estimated up to d/o 70) and triple-pair scenario 3pii,b (estimated up to d/o 90) in terms of an average of the seven-day solutions of the two-monthly observation period with either a co-estimated daily gravity field up to d/o 15 or 20. The daily gravity field solution based on the triple-pair scenario 3pii,b shows a significant improvement in the first 10 degrees (Figure 7b). If a higher degree is chosen, the limits of the double pair scenario become visible in the seven-day solution. For any higher daily solution, a triple-pair scenario is necessary to avoid spatial under-sampling.
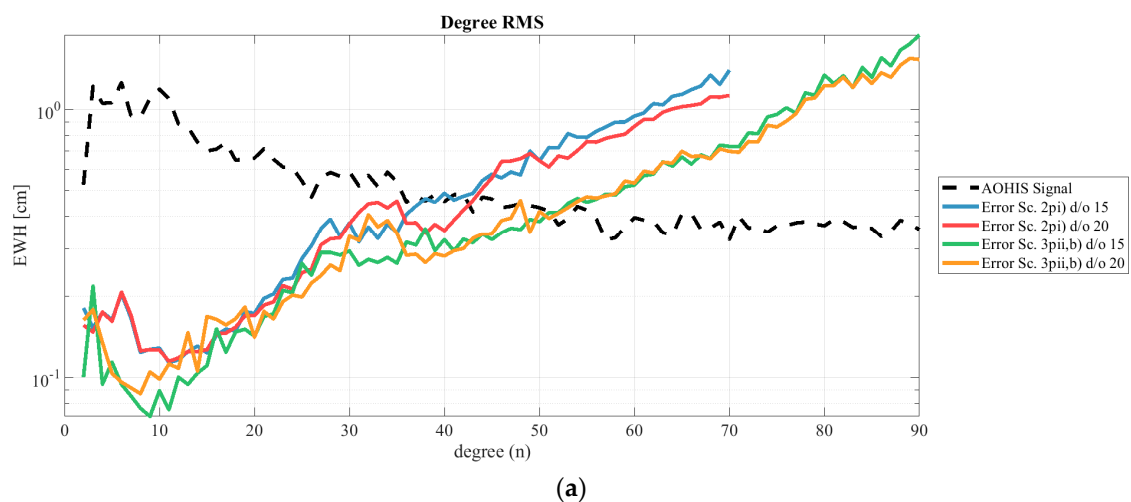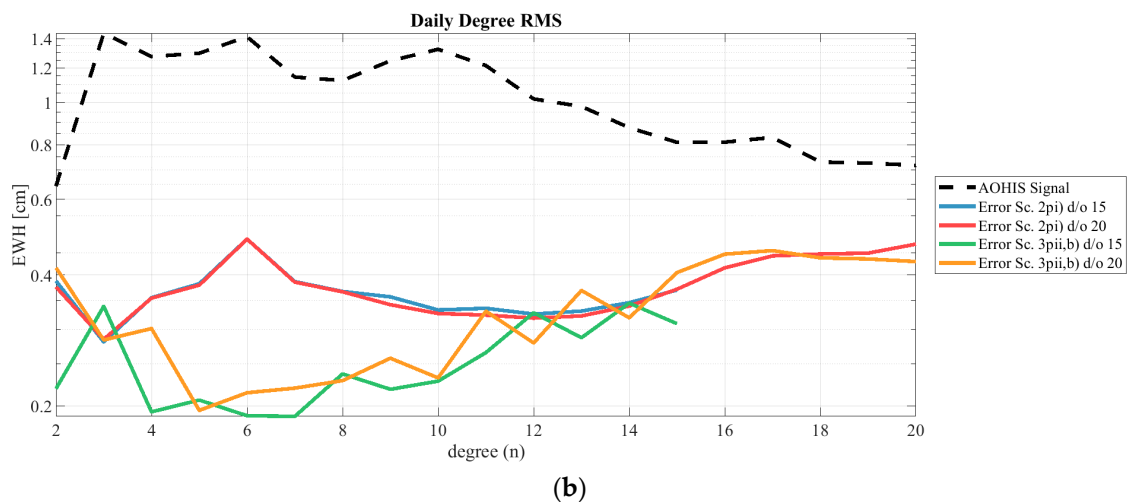

(**a**)

Figure 7. *Cont.*

(b)

Figure 7. Degree RMS of scenario 2pi and 3pii,b. (**a**) Seven-day solution degree RMS with daily parametrization up to d/o 15 and 20. (**b**) Degree RMS of daily solutions with parametrization up to d/o 15 and 20.

4.2. Higher-Degree Daily Resolution

As indicated, the most significant advantage of an additional pair is the expected improved performance of the daily solution. We chose the best-performing triple-pair scenario 3pii,b as the test scenario. The maximum daily degree and order varied between d/o 10 and d/o 40 with a step size of 5. Figure 8a shows the degree RMS of the overall solution, and Figure 8b shows the daily solution. In the overall solution, the nominal processing (without co-estimating daily gravity field parameters) is also included in red. When assessing the results of the daily solutions, the lowest daily d/o as well as the highest d/o are not recommended. When computing daily solution up to d/o 10, the result in Figure 8b shows clearly that the solution was under-parametrized and performed worst in the lower degrees. The daily solution up to d/o 20 performed best in the overall solution and should be preferred if the quality of the long-term solution has the highest priority. With a crossing point of the signal and error curve at approximately d/o 26, we recommend a daily parametrization up to d/o 25 or 30. The cumulative errors in Table 5 (without omission error) and Table 6 (including omission errors) confirm that the best solutions with the highest d/o are solutions 25 to 35, as they have the lowest error values at the investigated degrees (values marked with "1"). In Table 5, we used the AOHIS signal up to the respective SH degree of the solution as a reference, while the full AOHIS signal up to d/o 40 was used for the results shown in Table 6. Therefore, the first case provides only the commissioning error of the solutions, while the latter case includes also unresolved signals (omission error). The cumulative error of the daily solution estimated up to d/o 40 has the worst performance starting at d/o 25 (values marked with "2"). Considering the processing time, which increases with higher daily parametrization, and the performance of the daily solutions, the maximum daily d/o resolution should be chosen using the crossing point of the signal and error curves as a guideline.
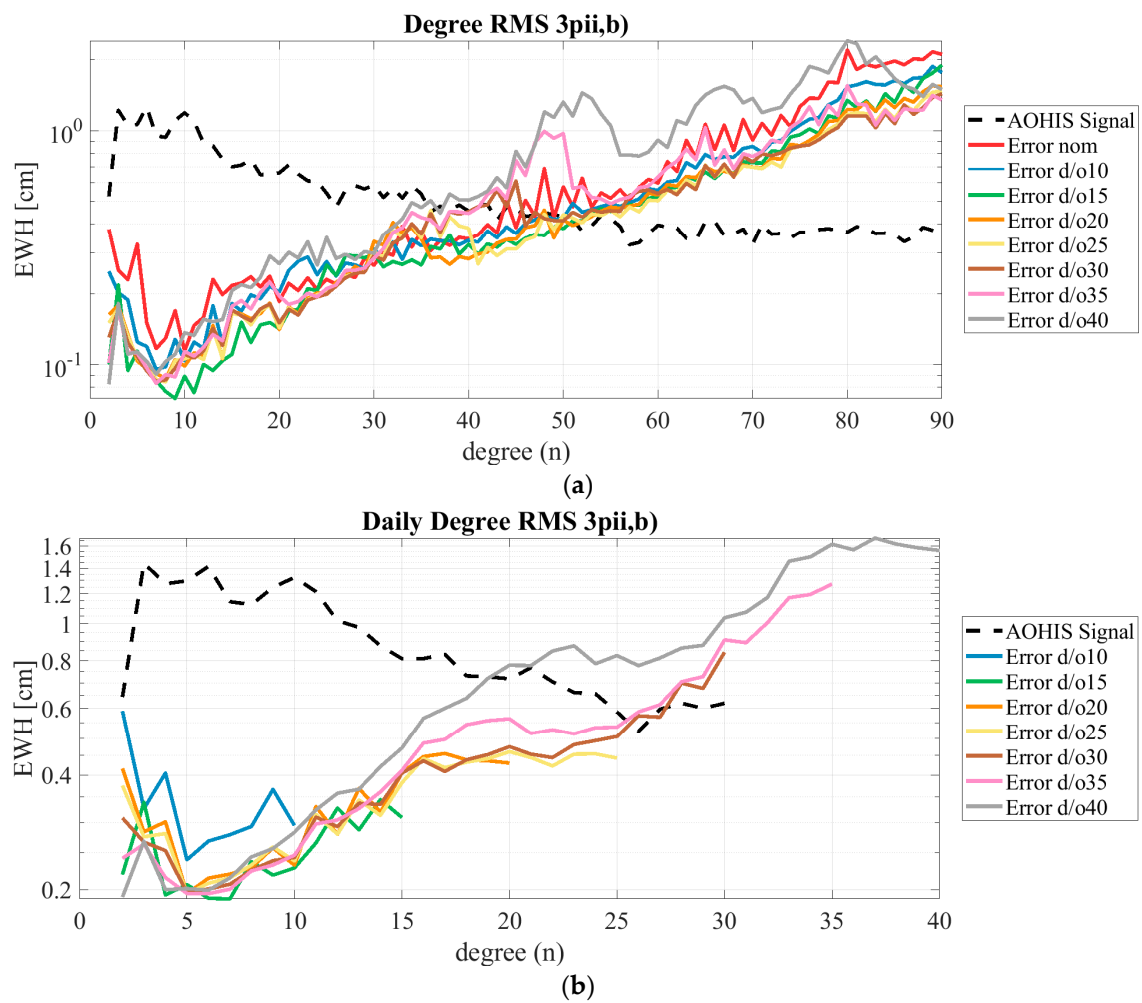
Figure 8. Degree RMS of scenario 3pii,b with different daily d/o. The nominal processing of the scenario is included as comparison. (**a**) Degree RMS average of the overall solutions, (**b**) Daily degree RMS average of the daily solutions. Compare to Table 5.

Table 5. Daily cumulative error of different daily solutions from scenario 3pii,b excluding omission error in cm EWH. Compare to Table 6. The best values are marked with "1". The values marked with "2" implicate an over-parametrization, impacting the result negatively.

Daily d/o \\ Cumulative Error at	d/o 10	15	20	25	30	35	40 in [cm] EWH
10	1.33	-	-	-	-	-	-
15	0.97	0.97	-	-	-	-	-
20	0.91	0.91	1.55	-	-	-	-
25	0.84	0.84	1.44 [1]	1.82 [1]	-	-	-
30	0.74	0.74	1.40 [1]	1.83 [1]	2.27 [1]	-	-
35	0.71	0.71	1.37 [1]	1.84 [1]	2.23 [1]	3.03	-
40	0.70	0.70	1.49	2.53 [2]	3.00 [2]	3.88 [2]	5.97

Table 6. Daily Cumulative error of different daily solutions from scenario 3pii,b including omission error (reference solution up to d/o 40) in cm EWH. Compare to Table 5. The best values are marked with "1". The values marked with "2" implicate an over-parametrization, impacting the result negatively.

Daily d/o \\ Cumulative Error at	d/o 10	15	20	25	30	35	40 in [cm] EWH
10	4.44	-	-	-	-	-	-
15	4.33	3.66	-	-	-	-	-
20	4.32	3.59	3.25	-	-	-	-
25	4.30	3.56	3.21 [1]	2.91 [1]	-	-	-
30	4.29	3.54	3.19 [1]	2.93 [1]	2.93 [1]	-	-
35	4.28	3.53	3.19 [1]	2.94 [1]	2.94 [1]	2.94	-
40	4.28	3.56	3.29	3.45[2]	3.45 [2]	3.45 [2]	3.45

To visualize the spatial difference of daily solutions from scenario 3pii,b with different maximum d/o, Figure 9 shows the daily temporal gravity field, as well the difference of daily solutions with different maximum d/o to the reference, for the whole Earth as well as exemplarily for a detail in the Northern Hemisphere over Europe and Africa. The reference gravity field is always used up to d/o 40 in order to include also the non-resolved signals. The increasing signal as well as the emerging error characteristics can be easily tracked among the different resolutions. The figure visualizes the importance of higher spatial resolution, as the details of the temporal gravity field are revealed. The last two rows with d/o 35 and 40 show an increased error, corresponding to the daily degree RMS in Figure 8b. The maximum daily d/o resolution of 40 demonstrates quite clearly the problems that emerge when the daily solution is over-parametrized. Additional constraints would be necessary to handle the arising spatial aliasing in the solution. Additionally, the solution pushes the numerical stability of the overall system to its limit and would potentially need additional constraints or a regularization scheme.
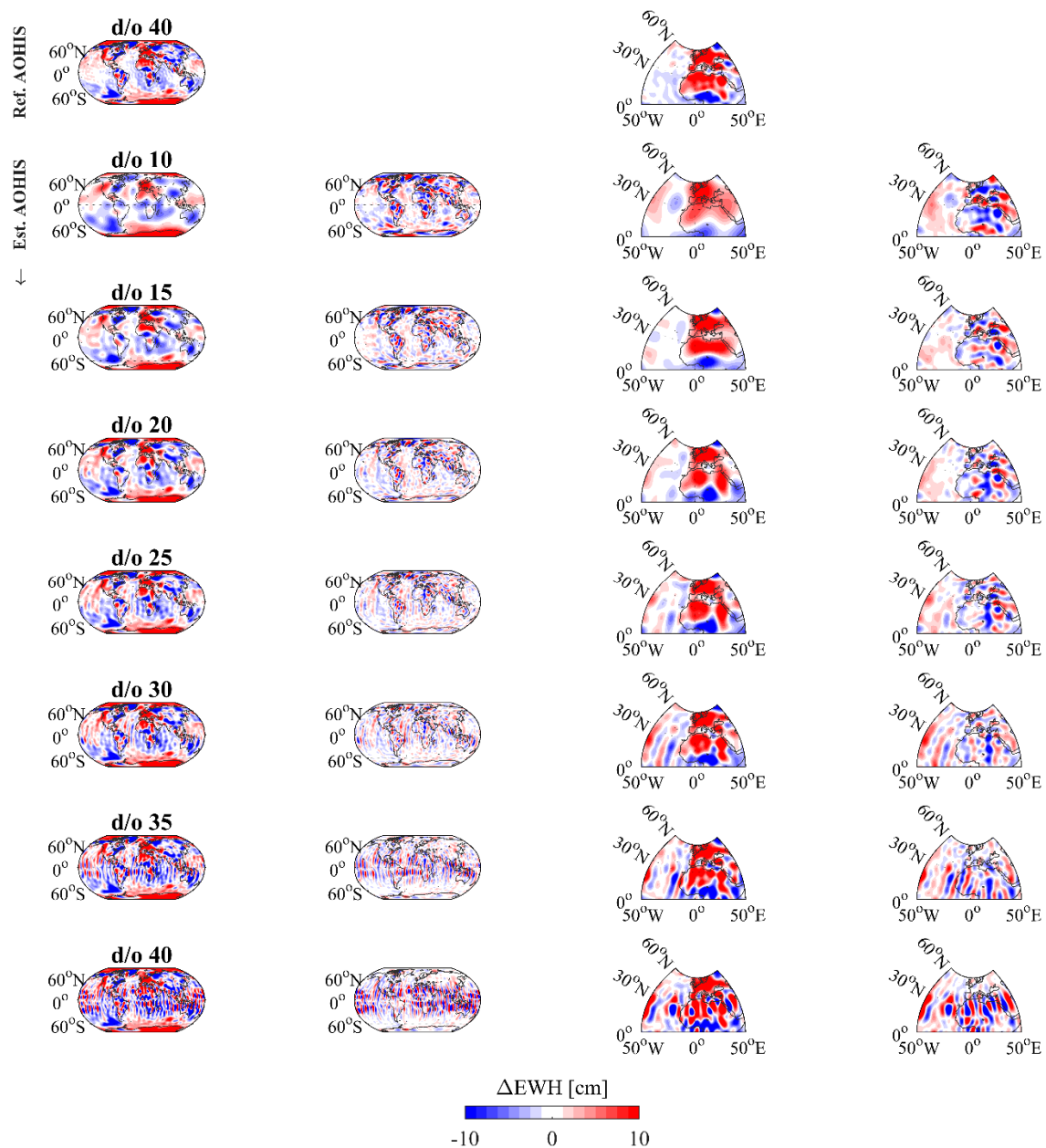
Figure 9. Spatial representation of the daily solutions for 11/01/2002 with different daily maximum degree based on scenario 3pii,p per row. Columns 1 and 3 show the estimated gravity field. Columns 2 and 4 show the difference to the reference atmosphere, ocean, hydrology, ice, and solid Earth (AOHIS) (d/o 40), such including the omission error. Columns 3 and 4 show a snapshot of the Northern hemisphere.

Figure 10 visualizes in the spatial domain the error of the gravity field combined with the ground track pattern for the daily solution up to d/o 30 and 40. As the ground track is designed to cover the Earth within a seven-day period optimally, the daily ground track coverage is not ideal. In Figure 10a,b, a daily solution parametrized up to d/o 30 is visualized and shows only a subtle striping pattern. In comparison, the parametrization up to d/o 40 in Figure 10c,d, shows the spatial aliasing, also very prominently visible in the detail picture of the Northern hemisphere in Figure 9. The error is especially dominant in areas that are not covered by ground tracks. Overall, the example shows that an optimal choice of the daily maximum degree is of great importance to the resulting daily gravity field.
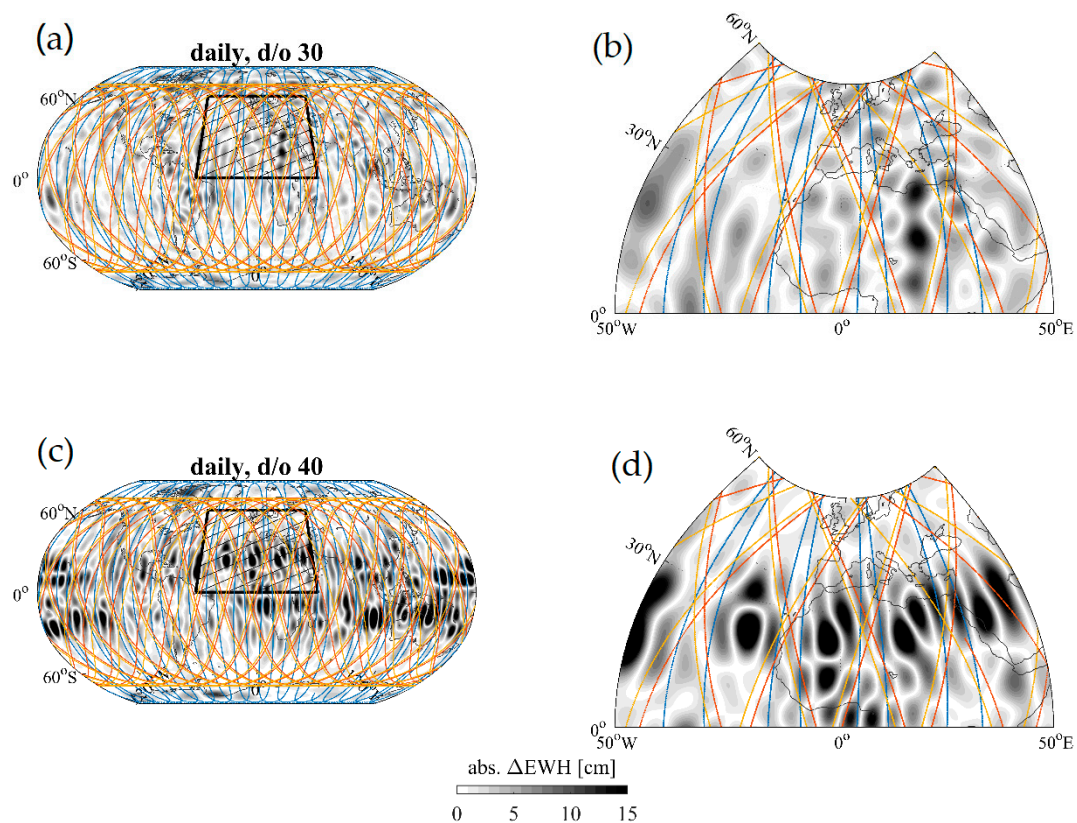
Figure 10. Spatial representation of daily solution (11/01/2002) and ground tracks. Global representation in first column, detail in column 2. (**a,b**) Solution up to d/o 30 (**c,d**); Solution up d/o 40. Omission error included.

4.3. Applications

For the assessment of the results regarding potential applications, we computed time series for a whole year based on scenario 2pi (computed up to d/o 70), 3pip,b, and 3pii,b (computed up to d/o 90) with daily solutions up to d/o 15, and retrieval periods of seven days. All values of the time series are retrieved from the respective coefficient estimates in the selected areas up to d/o 50. We selected and evaluated 12 areas listed in Table 7 with signals in hydrology and ice. The catchment and basins borders are used as boundaries. To cover various scenarios, five large catchments, five small catchments, and two ice drainage basins were selected. Figure 11 shows a time series in EWH for the Amazon region (a), the Danube catchment (b), a small part of California (c), and of the southwest (SW) of Greenland (d) over a whole year. As a reference, the AOHIS from the ESA ESM processed the same way is visualized in the dashed blue line. In the Amazon time series, the mass increase due to the rain period is detectable. The small catchment of the San Joaquin River in Southern California covers part of the drought area, as 2002 was one of the driest seasons since records are taken. As the catchment is rather small, an increased error is visible.

Table 7 summarizes the standard deviation of the differences of the solutions to their reference of the selected catchments and basins and of the three scenarios. Also, the gain of the triple-pair scenarios compared to the double pair scenario is determined. The gain is the standard deviation difference with the standard deviation of the double pair, multiplied by 100. It shows that the second polar pair gave a smaller benefit in average 10.7%, while the second inclined pair improved on average by 21%. One of the examples of Greenland shows that the gain is even visible in areas, where the inclined pair does not add observations. When only evaluating the big catchment, both triple-pair scenarios perform similar with more than 20% improvement. When investigating the small catchments, however, the performance of the triple-pair scenario 3pip,b declines to a small improvement only of 5%, while

scenario 3pii,b has the same improvement as for the big catchments (cf. Table 7). In the ice drainage basins, triple pair 3pip,b performs even worse than the double pair.
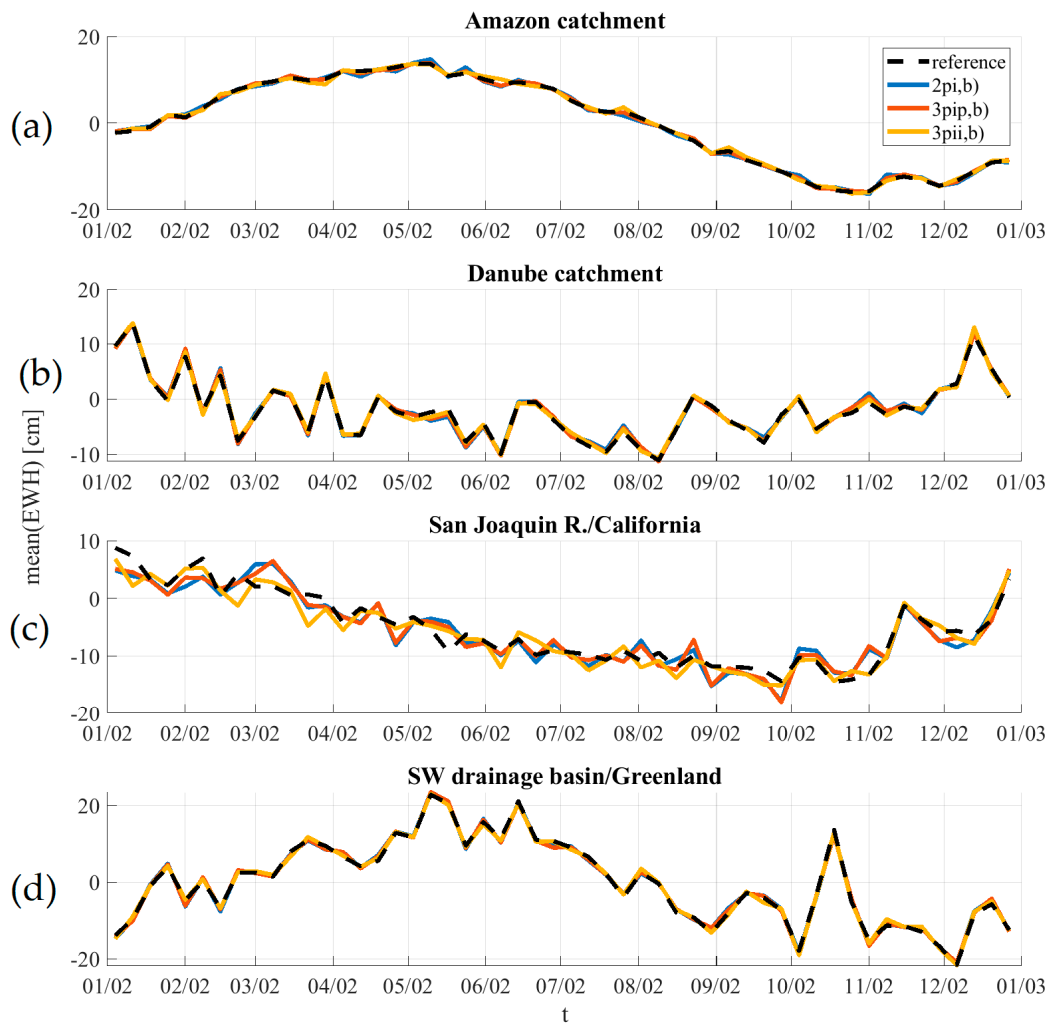

Figure 11. Time series for four selected catchments in EWH (cm) (**a**) Amazon basin, (**b**) Danube basin, (**c**) San Joaquin River/California, (**d**) South-East drainage basin/Greenland extracted from seven-day solutions up to d/o 50 based on scenario 2pi, 3pip,b, and 3pii,b. Compare to Table 7. Daily Wiese solution co-parametrized up to d/o 15.

Table 7. Standard deviation of Scenario 2pi, 3pip,b, and 3pii,b up d/o 50 (with daily d/o 15) and the gain of the triple-pair scenarios compared to the double pair scenario. Computed over one year of the indicated catchments in cm EWH. Clustered: Big catchments, small catchments, ice drainage basins according to the Rignot basins, IMBIE project (http://imbie.org/imbie-2016/drainage-basins/). Additionally, in the last two columns are the standard deviation of daily solutions based on Scenario 3pii,b, once co-estimated up to d/o 15 and once co-estimated up to d/o 25.

Catchment \\ Scenario	2pi Std. [cm]	3pip,b Std. [cm]	Gain [%]	3pii,b Std. [cm]	Gain [%]	d/o 15 Std. [cm]	d/o 25 Std. [cm]
Mississippi	0.57	0.53	7.3	0.41	28.3	0.90	0.91
Amazon	0.56	0.29	48.3	0.43	23.1	0.71	0.65
Danube	0.65	0.54	16.9	0.46	29.9	0.89	1.04
Yangtze R.	0.66	0.49	25.9	0.59	9.7	0.73	0.71
Ganges	0.66	0.55	17.5	0.54	18.5	0.98	1.04
San Joaquin R.	2.24	2.08	7.2	1.81	18.9	1.13	1.79
Fitzroy R.	3.43	3.35	2.3	2.45	28.5	1.27	3.14
Elbe	2.49	2.29	7.8	1.70	31.6	1.03	1.38
Dead sea	2.22	2.13	4.4	1.90	14.8	1.17	1.77
Upper Mississippi	1.79	1.73	3.4	1.26	29.7	1.39	1.77
SW Greenl.	0.79	0.77	2.3	0.63	20.3	1.05	0.91
NE Greenl.	0.97	1.11	−14.8	0.97	−0.4	0.82	1.30
Average	**1.42**	**1.32**	**10.7**	**1.10**	**21.1**	**1.01**	**1.39**

Based on scenario 3pii,b, a scenario with daily solution co-estimated up to d/o 25 was also computed, to analyze the possibility of a higher daily solution. Figure 12 therefore visualizes the daily solutions up to d/o 15 and 25 from scenario 3pii,b for the Danube catchment and the ice drainage basin in SW Greenland over two months. The corresponding standard deviations can be found in Table 7. In both examples, a difference between the d/o 15 and 25 curve is visible and can be explained by the omission error. Figure 13 compares the seven-day solution to the d/o 25 daily solution. In the Greenland example (b), both curves have the same base characteristics. However, in the daily curve, the omission error is visible, as the curve is missing signal amplitude. The Danube time series (a) in comparison visualizes the fact that the daily solution has the same signal strength and adds additional time-variable information. Both examples in Figure 13 show that both daily and weekly solutions have advantages, depending on the characteristic of the underlying geophysical signals. Based on the individual applications demand, the spatial and temporal resolutions have to be balanced.
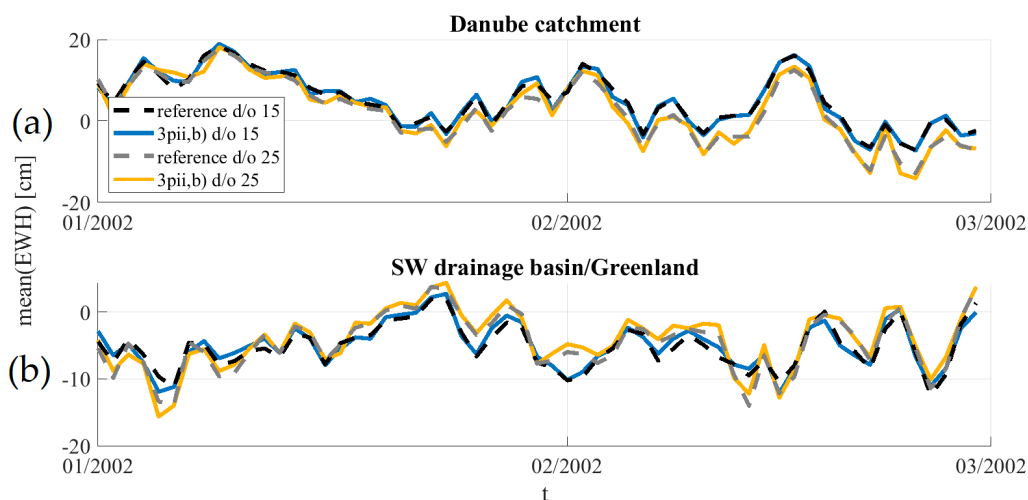

Figure 12. Time series in EWH (cm) for Danube catchment (**a**) and SW drainage basin in Greenland (**b**) of Scenario 3pii,b extracted from daily solutions with d/o 15 and 25. Two-month period extracted from the one year processed.
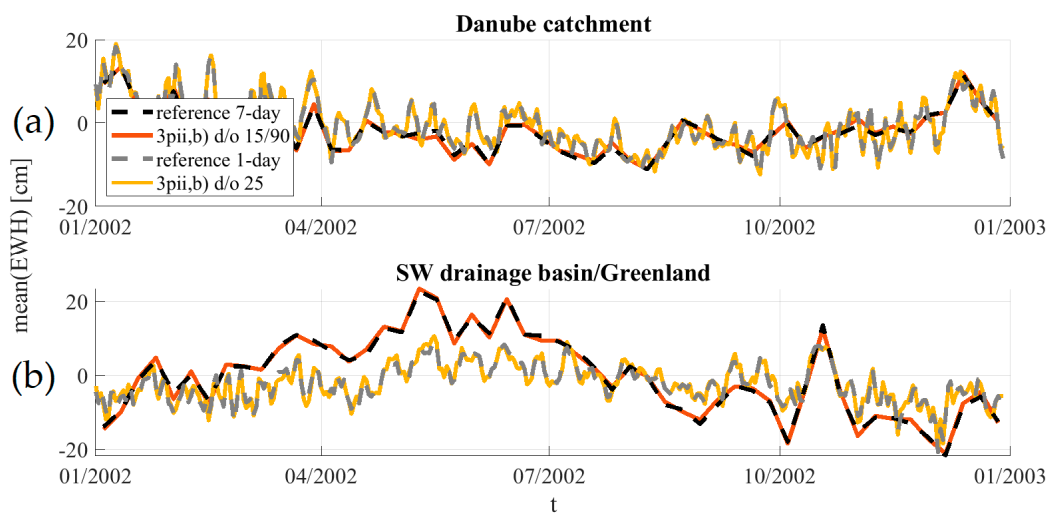
Figure 13. Time series in EWH (cm) for Danube catchment (**a**) and SW drainage basin in Greenland (**b**) of Scenario 3pii,b comparing daily solutions (d/o 25) to the signal content of the seven-day solution up to d/o 50 of scenario 3pii,b for one year.

In Figure 14, the magnitude of the daily signal of the SW Greenland example due to the omission error was improved by adding a three-day solution (computed based on the same scenario) starting at the highest d/o of the daily solution (see [28]). This means up to d/o 25 the daily solution was used, artificially enhanced by the three-day solution starting d/o 26 to the maximum degree of 50. As [28] showed, this approach does not significantly distort the daily solution, while at the same time, it adds information with long-wavelength frequency content. Part of the omission error, therefore, can be reduced.
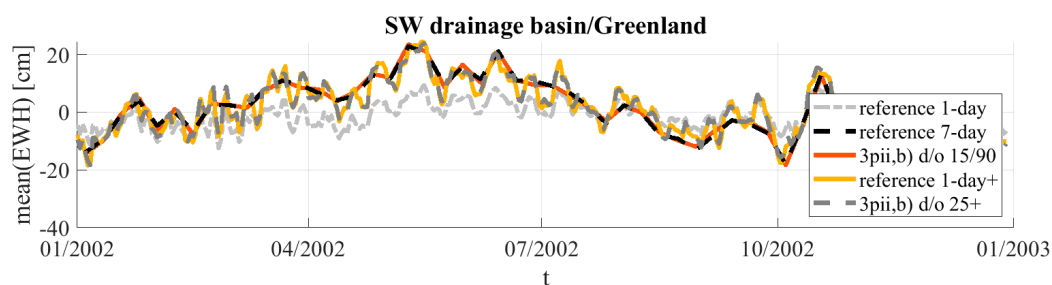

Figure 14. Time series in EWH (cm) for SW Greenland ice drainage basin based on Scenario 3pii,b comparing daily solutions (d/o 25) plus three-day solution (indicated by the "+") up to 50 to the signal content of the seven-day solution up to d/o 50 of scenario 3pii,b for one year. The reference solution of the former daily solution is visualized in a light grey for comparison.

5. Conclusions

With our closed-loop simulation software, we tested the impact of a third satellite in an inclined or near-polar orbit with GRACE-like or NGGM instrument noise specifications. As the base scenario, we used a Bender-type double-pair constellation. While the second pair, as demonstrated by, e.g., [26], has the added benefit of enhanced de-striping capabilities and further allows the observation of the full AOHIS, we showed that the impact of an additional third satellite pair is between 5% and 40%. Compared with the expected 22% improvement of the square-root-n rule, this indicates that the additional polar pair does add redundant information, while the third pair in the inclined orbit adds significant observations. Our tests also revealed a dampened striping effect and an improved error RMS variability. The third pair in an inclined orbit is preferable compared to the third pair in a polar orbit. The best third pair option is an inclined pair with improved NGGM instrumentation. Therefore,

we recommend flying an inclined pair, to add not only additional observations, but also a different observation geometry. The error curve of the daily triple pair gravity field meets the signal curve at approximately degree 26. Our tests confirmed that the processing up to d/o 30 is beneficial, while a higher parametrization adds spatial aliasing to the solution. We therefore note that it is crucial to choose the daily maximum degree with care.

To test the best triple-pair scenarios for applications, we extended the time series towards one year. We looked into typical regions regarding hydrology and ice like the Amazon catchment, the Danube basin, or Greenland. Compared to the Bender double pair scenario, the gain of the third pair in a polar orbit is on average 11%, while adding a third pair in an inclined orbit exhibits a gain of approximately 21%, which is achievable for bigger as well as small catchments. Especially the visualized SW Greenland time series demonstrates the importance of a high d/o daily solution, as the omission error in the region can be significant. The tested approach to add higher d/o long-term solutions onto daily solutions as presented in [28] improves the results significantly and can be recommended as methodology for future applications.

As a conclusion, while the benefit of a Bender-type double-pair constellation over a single-pair GRACE like concept is substantial, we can state that a third pair improves the achievable performance of a double pair constellation only moderately. Our results also suggest that an inclined third pair would be the better option to improve the overall performance.

References

1. Reigber, C.; Schwintzer, P.; Lühr, H. The CHAMP geopotential mission, Bollettino di Geofisica Teoretica ed Applicata, 40/ 3-4, September-December 1999. In Proceedings of the Second Joint Meeting of the International Gravity and the International Geoid Commission, Trieste, Italy, 7–12 September 1998; Marson, I., Sünkel, H., Eds.; 1999; pp. 285–6729, ISSN 0006-6729.
2. Tapley, B.D.; Bettadpur, S.; Watkins, M.; Reigber, C. The gravity recovery and climate experiment experiment, mission overview and early results. *Geophys. Res. Lett.* **2004**, *31*, L09607. [CrossRef]
3. Kornfeld, R.P.; Arnold, B.W.; Gross, M.A.; Dahya, N.T.; Klipstein, W.M.; Gath, P.F.; Bettadpur, S. GRACE-FO: The Gravity Recovery and Climate Experiment Follow-On Mission. *J. Spacecr. Rocket.* **2019**, *56*, 931–951. [CrossRef]
4. Rodell, M.; Famiglietti, J.S.; Wiese, D.N.; Reager, J.T.; Beaudoing, H.K.; Landerer, F.W.; Lo, M.H. Emerging trends in global freshwater availability. *Nature* **2018**, *557*, 651–659. [CrossRef]
5. Forootan, E.; Didova, O.; Schumacher, M.; Kusche, J.; Elsaka, B. Comparisons of atmospheric mass variations derived from ECMWF reanalysis and operational fields over 2003–2011. *J. Geod.* **2014**, *88*, 503–514. [CrossRef]
6. Panet, I.; Pajot-Métivier, G.; Greff-Lefftz, M.; Métivier, L.; Diament, M.; Mandea, M. Mapping the mass distribution of Earth's mantle using satellite-derived gravity gradients. *Nat. Geosci.* **2014**, *7*, 131–135. [CrossRef]
7. Han, S.; Riva, R.; Sauber, J.; Okal, E. Source parameter inversion for recent great earthquakes from a decade-long observation of global gravity fields. *J. Geophys. Res.* **2013**, *118*, 1240–1267. [CrossRef]
8. Ivins, E.; Watkins, M.; Yuan, D.N.; Dietrich, R.; Casassa, G.; Rülke, A. On land ice loss and glacial isostatic adjustment at the Drake Passage: 2003–2009. *J. Geophys. Res.* **2011**, *116*, B02403. [CrossRef]

9. Luthcke, S.B.; Sabaka, T.; Loomis, B.; Arendt, A.; McCarthy, J.; Camp, J. Antarctica, Greenland, and Gulf of Alaska land-ice evolution from an iterated GRACE global mascon solution. *J. Geophys.* **2013**, *59*, 613–631. [CrossRef]

10. Velicogna, I.; Sutterley, T.C.; van den Broeke, M.R. Regional acceleration in ice mass loss from Greenland and Antarctica using GRACE time-variable gravity data. *Geophys. Res. Lett.* **2014**, *41*, 8130–8137. [CrossRef]

11. Pail, R.; Bingham, R.; Braitenberg, C.; Dobsalw, H.; Eicker, A.; Güntner, A.; Horwarth, M.; Ivins, E.; Longuevergne, L.; Panet, I.; et al. IUGG Expert Panel Science and User Needs for Observing Global Mass Transport to Understand Global Change and to Benefit Society. *Surv. Geophys.* **2015**, *36*. [CrossRef]

12. Sharifi, M.; Sneeuw, N.; Keller, W. Gravity recovery capability of four generic satellite formations. In Proceedings of the 1st International Symposium of the International Gravity Field Sevice "Gravity Field of the Earth". *Gen. Command Mapp.*, Istanbul, Turkey, 28 August–1 September 2007; Kilicoglu, A., Forsberg, R., Eds.; 2007; pp. 211–216, ISSN 1300-5790.

13. Sneeuw, N.; Sharifi, M.; Keller, M. Gravity Recovery from Formation Flight Missions. VI Hotine-Marussi Symposium on Theoretical and Computational Geodesy. *Sensors* **2008**, *132*, 29–34. [CrossRef]

14. Wiese, D.N.; Folkner, W.M.; Nerem, R.S. Alternative mission architectures for a gravity recovery satellite mission. *J. Geod.* **2008**, *83*, 569–581. [CrossRef]

15. Elsaka, B.; Kusche, J.; Ilk, K.-H. Recovery of the Earth's Gravity Field from Formation-Flying Satellites: Temporal Aliasing Issues. *Adv. Space Res.* **2012**, *50*, 1534–1552. [CrossRef]

16. Iran Pour, S.; Reubelt, T.; Sneeuw, N.; Daras, I.; Murböck, M.; Gruber, T.; Pail, R.; Weigelt, M.; van Dam, T.; Visser, P.; et al. *Assessment of Satellite Constellations for Monitoring the Variations in Earth Gravity field–SC4MGV, ESA–ESTEC Contract No. AO/1-7317/12/NL/AF, Final Report*; ESA-ESTEC: Noordwijk, Netherlands, 2015.

17. Bender, P.L.; Wiese, D.; Nerem, R.S. A Possible Dual-GRACE Mission with 90 Degree and 63 Degree Inclination Orbits. In Proceedings of the 3rd International Symposium on Formation Flying, Missions and Technologies, ESA/ESTEC, Noordwijk, The Netherlands, 23–25 April 2008.

18. Wiese, D.; Nerem, R.; Han, S.-C. Expected Improvements in Determining Continental Hydrology, Ice Mass Variations, Ocean Bottom Pressure Signals, and Earthquakes Using Two Pairs of Dedicated Satellites for Temporal Gravity Recovery. *J. Geophys. Res.* **2011**, *116*, 405. [CrossRef]

19. Wiese, D.; Nerem, R.; Lemoine, F. Design considerations for a dedicated gravity recovery satellite mission consisting of two pairs of satellites. *J. Geophys.* **2012**, *86*, 81–98. [CrossRef]

20. Daras, I.; Pail, R. Treatment of temporal aliasing effects in the context of next generation satellite gravimetry missions. *J. Geophys. Res.* **2017**, *22*, 7343–7362. [CrossRef]

21. Panet, I.; Flury, J.; Biancale, R.; Gruber Th Johannessen, J.; Van den Broeke, M.; Van Dam, T.; Gegout, P.; Hughes Ch Ramillien, G.; Sasgen, I.; Seoane, L.; et al. Earth System Mass Transport Mission (e.motion): A Concept for Future Earth Gravity Field Measurements from Space. *Surv. Geophys.* **2012**. [CrossRef]

22. Gruber, T.; Murböck, M.; NGGM-D Team. *e2.Motion-Earth System Mass Transport Mission (Square)-Concept for a Next Generation Gravity Field Mission*; DGK, Reihe B, 318; Verlag C.H. Beck: Munich, Germany, 2014.

23. Pail, R.; Bamber, J.; Biancale, R.; Bingham, R.; Braitenberg, C.; Eicker, A.; Flechtner, F.; Gruber, T.; Güntner, A.; Heinzel, G.; et al. Mass variation observing system by high low inter-satellite links (MOBILE)–a new concept for sustained observation of mass transport from space. *J. Geod. Sci.* **2019**, *9*, 48–58. [CrossRef]

24. Elsaka, B.; Raimondo, J.-C.; Brieden Ph Reubelt, T.; Kusche, J.; Flechtner, F.; Iran Pour, S.; Sneeuw, N.; Müller, J. Comparing Seven Candidate Mission Configurations for Temporal Gravity Retrieval through Full-Scale Numerical Simulation. *J. Geophys.* **2014**, *88*, 31–43. [CrossRef]

25. Purkhauser, A.F.; Pail, R.; Hauk, M.; Visser, P.; Sneeuw, N.; Saemian, P.; Liu, W.; Engels, J.; Chen, Q.; Siemes, C.; et al. Gravity Field Retrieval of Next Generation Gravity Missions regarding Geophysical Services: Results of the ESA-ADDCON Project. European Geosciences Union General Assembly 2018. Available online: https://meetingorganizer.copernicus.org/EGU2018/EGU2018-2770.pdf (accessed on 4 March 2020).

26. Purkhauser, A.; Siemes, C.; Pail, R. Consistent quantification of the impact of key mission design parameters on the performance of next-generation gravity missions. *Geophys. J. Int.* **2020**, *221*, 1190–1210. [CrossRef]

27. Wiese, D.N.; Visser, P.; Nerem, R.S. Estimating low resolution gravity fields at short time intervals to reduce temporal aliasing errors. *Adv. Space Res.* **2011**, *48*, 1094–1107. [CrossRef]

28. Purkhauser, A.F.; Pail, R. Next generation gravity missions: Near-real time gravity field retrieval strategy. *Geophys. J. Int.* **2019**. [CrossRef]

29. Visser, P.M.A.M.; Schrama, E.J.O.; Sneeuw, N.; Weigelt, M. Dependency of Resolvable Gravitational Spatial Resolution on Space-Borne Observation Techniques. *Int. Assoc. Geodesy Symposia* **2011**, 373–379. [CrossRef]

30. Weigelt, M.; Sneeuw, N.; Schrama, E.; Visser, P. An improved sampling rule for mapping geopotential functions of a planet from a near polar orbit. *J. Geophys.* **2012**, *87*. [CrossRef]

31. Sneeuw, N.; Flury, J.; Rummel, R. Science Requirements on Future Missions And Simulated Mission Scenarios. *Future Satell. Gravim. Earth Dyn.* **2005**, 113–142. [CrossRef]

32. Swenson, S.; Wahr, J. Post-Processing removal of correlated errors in GRACE data. *Geophys. Res. Lett.* **2006**, *33*, L08402. [CrossRef]

33. Horvath, A.; Murböck, M.; Pail, R.; Horwath, M. Decorrelation of GRACE time variable gravity field solutions using full covariance information. *Geosciences* **2018**, *8*, 323. [CrossRef]

34. Kusche, J. Approximate decorrelation and non-isotropic smoothing of time-variable GRACE-type gravity field models. *J. Geophys.* **2007**, *81*, 733–749. [CrossRef]

35. Daras, I. Gravity Field Processing Towards Future LL-SST Satellite Missions; Deutsche Geodätische Kommission der Bayerischen Akademie der Wissenschaften, Reihe C. Ph.D.Thesis, Technische Universität München, München, Germany, 2016.

36. Daras, I.; Pail, R.; Murböck, M.; Yi, W. Gravity field processing with enhanced numerical precision for LL-SST missions. *J. Geophys.* **2015**, *89*, 99–110. [CrossRef]

37. Shampine, L.F.; Gordon, M.K. *Computer Solution of Ordinary differential Equations: The Initial Value Problem*; W.H. Freeman: San Francisco, CA, USA, 1975.

38. Montenbruck, O.; Gill, E. Satellite orbits: Models, methods, and applications. *Appl. Mech. Rev.* **2002**, *55*, B27–B28. [CrossRef]

39. Mayer-Gürr, T.; Pail, R.; Gruber, T.; Fecher, T.; Rexer, M.; Schuh, W.D.; Kusche, J.; Brockmann, J.M.; Rieser, D.; Zehentner, N.; et al. The combined satellite gravity field model GOCO05s. *Geophys. Res. Abstr.* **2015**, *17*. [CrossRef]

40. Dobslaw, H.; Bergmann-Wolf, I.; Dill, R.; Forootan, E.; Klemann, V.; Kusche, J.; Sasgen, I. The updated ESA Earth System Model for future gravity mission simulation studies. *J. Geophys.* **2015**, *89*, 505–513. [CrossRef]

41. Ray, R.D. *A Global Ocean tide Model from Topex/Poseidon Altimetry: Got99.2*; Technology report; NASA Technical Memorandum: NASA/TM-1999-209478; Goddard Space Flight Center: Greenbelt, MD, USA, 1999; p. 209478.

42. Savcenko, R.; Bosch, W. *EOT11a–Empirical Ocean Tide Model from Multi-Mission Satellite Altimetry*; DGFI Report: München, Germany, 2012.

43. Hofmann-Wellenhof, B.; Moritz, H. *Physical Geodesy*, 2nd ed.; Springer: Berlin/Heidelberg, Germany, 2012.

44. Pail, R.; Bruinsma, S.; Migliaccio, F.; Förste, C.; Goiginger, H.; Schuh, W.D.; Höck, E.; Reguzzoni, M.; Brockmann, J.M.; Abrikosov, O. First GOCE gravity field models derived by three different approaches. *J. Geophys.* **2011**, *85*, 819–843. [CrossRef]

45. Cheng, M.K.; Tapley, B.D. Seasonal variations in low degree zonal harmonics of the Earth's gravity field from satellite laser ranging observation. *J. Geophys. Res.* **1999**, *104*, 2667–2681. [CrossRef]

46. Touboul, P.; Metris, G.; Selig, H.; Le Traon, O.; Bresson, A.; Zahzam, N.; Christophe, B.; Rodrigues, M. Gravitation and Geodesy with Inertial Sensors, from Ground to Space. *Test. Aerosp. Res.* **2016**, *12*. [CrossRef]

47. Schrama EJO, Wouters B, Lavallée Signal and noise in Gravity Recovery and Climate Experiment (GRACE) observed surface mass variation. *J. Geophys. Res.* **2007**, *116*, B02407. [CrossRef]

48. Wahr, J.; Moleneer, M.; Bryan, F. Time variability of the Earth's gravity field: Hydrological and oceanic effets and their possible detection using GRACE. *J. Geophys. Res.* **1998**, *201*. [CrossRef]